

Statistical Modeling of 4D Respiratory Lung Motion Using Diffeomorphic Image Registration

Jan Ehrhardt*, René Werner, Alexander Schmidt-Richberg, and Heinz Handels

Abstract—Modeling of respiratory motion has become increasingly important in various applications of medical imaging (e.g., radiation therapy of lung cancer). Current modeling approaches are usually confined to intra-patient registration of 3D image data representing the individual patient's anatomy at different breathing phases. We propose an approach to generate a mean motion model of the lung based on thoracic 4D computed tomography (CT) data of different patients to extend the motion modeling capabilities. Our modeling process consists of three steps: an intra-subject registration to generate subject-specific motion models, the generation of an average shape and intensity atlas of the lung as anatomical reference frame, and the registration of the subject-specific motion models to the atlas in order to build a statistical 4D mean motion model (4D-MMM). Furthermore, we present methods to adapt the 4D mean motion model to a patient-specific lung geometry. In all steps, a symmetric diffeomorphic nonlinear intensity-based registration method was employed. The Log-Euclidean framework was used to compute statistics on the diffeomorphic transformations. The presented methods are then used to build a mean motion model of respiratory lung motion using thoracic 4D CT data sets of 17 patients. We evaluate the model by applying it for estimating respiratory motion of ten lung cancer patients. The prediction is evaluated with respect to landmark and tumor motion, and the quantitative analysis results in a mean target registration error (TRE) of 3.3 ± 1.6 mm if lung dynamics are not impaired by large lung tumors or other lung disorders (e.g., emphysema). With regard to lung tumor motion, we show that prediction accuracy is independent of tumor size and tumor motion amplitude in the considered data set. However, tumors adhering to non-lung structures degrade local lung dynamics significantly and the model-based prediction accuracy is lower in these cases. The statistical respiratory motion model is capable of providing valuable prior knowledge in many fields of applications. We present two examples of possible applications in radiation therapy and image guided diagnosis.

Index Terms—Diffeomorphic registration, motion modeling, respiratory motion, statistical atlas generation, 4D computed tomography (CT).

I. INTRODUCTION

WITH 4D imaging techniques spatiotemporal image sequences can be acquired to investigate dynamic processes in the patient's body. For instance, respiratory correlated spatiotemporal computed tomography scans (4D CT) open up the possibility to research respiratory induced organ motion.

Manuscript received May 21, 2010; revised August 26, 2010; accepted August 27, 2010. Date of publication September 27, 2010; date of current version February 02, 2011. Asterisk indicates corresponding author.

*J. Ehrhardt is with the Institute of Medical Informatics, University of Lübeck, 23538 Lübeck, Germany (e-mail: ehrhardt@imi.uni-luebeck.de).

R. Werner, A. Schmidt-Richberg, and H. Handels are with the Institute of Medical Informatics, University of Lübeck, 23538 Lübeck, Germany.

Digital Object Identifier 10.1109/TMI.2010.2076299

The clinical relevance of this research is diverse. Respiratory motion is related to the function of the lung and therefore a diagnostic value in itself. Furthermore, breathing induced organ motion potentially leads to image artifacts and to position uncertainty in image guided procedures. Particularly in radiotherapy planning of thoracic and abdominal tumors, the respiratory motion causes important uncertainties and is a significant source of error [1]. Therefore, there has been a large and continuing growth in studies and applications of 4D CT images for motion measurement, radiotherapy treatment planning, as well as functional investigations [2]–[5]. The role of image registration techniques is increasing in these applications. Image registration enables the estimation of the breathing-induced motion and the description of the temporal change in position and shape of the structures of interest by establishing the correspondence between images acquired at different phases of the breathing cycle. A variety of image registration approaches have been used for respiratory motion estimation in recent years (see [6] for a review).

In radiotherapy estimations are used to define accurate treatment margins, to calculate dose distributions and to develop prediction models for gated or robotic radiotherapy. However, the computed motion models are confined to the individual breathing cycle represented in the 4D image data. The problem of these methods is the presupposition that the breathing motion is reproducible throughout image acquisition, radiotherapy planning, and the delivery process of treatment. It has been shown that breathing motion is not a robust and 100% reproducible process [7], [8] and a widespread consensus now exists that it would be useful to use prior knowledge of respiratory organ motion and its variability to improve radiotherapy planning and treatment delivery [9].

Some motion modeling approaches have been published that deal with the variations of breathing motion. Low *et al.* [10] describe a motion model of the lung parametrized by tidal volume and airflow measured with spirometry. This allows to model hysteresis and irregular breathing patterns. McClelland *et al.* [11] compute an average respiratory cycle by fitting a periodic B-spline function to the trajectory of a target point (voxel). The effects of variation between different cycles are reduced and a memory-efficient, time-continuous model is generated. Coolens *et al.* [12] describe a new treatment margin concept that addresses breathing motion variations. An elliptic model is fitted to the target trajectory and the deviations from the elliptic trajectory in position and phase are used for an appropriate margin formulation. These approaches have in common that the parameters of a predefined motion model are estimated from motion information extracted from 4D images.

In contrast, Neicu *et al.* [13] computes a mean tumor trajectory and phase by averaging the breathing cycle periods and the phase-dependent tumor positions.

The approach proposed in this paper is different from the previous methods in several ways. Our approach does not rely on a predefined model whose parameters are fitted to match specific data. Instead, our motion model constitutes the *statistical* mean of the motion extracted from 4D images. The previous methods consider each target point independently for parameter estimation or average calculation. In our approach, the deformation of the whole organ between different breathing phases, e.g., from start inhale to mid-inhale, is regarded as a nonlinear diffeomorphic transformation of the 3D space, and statistics are performed on a population of such transformations. Furthermore, the methods mentioned before focus on the generation of intra-patient models. In this paper, methods are presented to generate a statistical inter-patient 4D motion model of the lung from a population of 4D images of different patients.

Statistical inter-patient motion models have been constructed before for myocardial motion. In [14] and [15], nonlinear registration methods were used for the estimation of subject-specific cardiac motion and for the spatio-temporal alignment of MR sequences of different subjects into a common reference coordinate system. The subject-specific motion fields were transferred into the reference coordinate system by the algorithm proposed in [16] and a statistical myocardial motion analysis was performed. The first steps towards an average inter-patient lung motion model were done by Sundaram *et al.* [17], but their work focuses on the temporal reparametrization of $2D + t$ lung MR images and the generation of average intensity images for corresponding breathing states.

Our modeling approach is based on the assumption that breathing dynamics work similarly for all patients examined. Starting from 4D CT images and associated lung segmentation masks from different patients acquired during free breathing, methods are presented to extract an average shape and intensity atlas of the lung (used as anatomical reference frame) and to generate a statistical model of the mean lung motion. In contrast to previous work [14], [15], the breathing motion of each subject is represented by a sequence of diffeomorphic transformations. The computed motion fields of different subjects are then transformed into the atlas coordinate system. Thus, a statistical inter-patient analysis of the motion fields becomes possible, differences in respiratory motion between patients can be quantified and analyzed, and further insights into the variability of breathing motion between individuals can be achieved. A statistical 4D mean motion model is generated from the population of sequences of diffeomorphisms. Such a statistical model of the respiratory motion can provide valuable prior knowledge in many fields of application, e.g., for dose calculation in radiation therapy, to reduce motion-related artifacts during image acquisition, or to improve the robustness and precision of motion estimation algorithms. The reliability of our approach is demonstrated by using the motion model for predicting respiratory motion of individual patients and evaluating the prediction quality.

Essential for our work is the development of the Log-Euclidean framework, recently proposed by Arsigny *et al.* [18].

The Log-Euclidean framework enables the implementation of efficient algorithms for nonlinear diffeomorphic registration [19] and provides a simple way for computing statistics on diffeomorphisms via *vectorial* statistics on their logarithms [20]. In contrast to other diffeomorphic registration approaches [21] and statistical methods based on Riemannian metrics [22], the computational costs are significantly reduced so that the processing of large image data sets is enabled. Furthermore, the inverse of the computed transformations is immediately known and thus the spatial transformation of motion fields is simpler and tends to be more straight forward than the algorithm proposed in [16].

The paper is structured as follows. In Section II the acquisition of the 4D CT images, the diffeomorphic registration methods and the computation of the average shape and motion model are described. Furthermore, methods for utilization of the 4D-MMM for motion prediction and evaluation methods are presented. In Section III, the average lung motion model is applied to predict lung and tumor motion for individual patients and compared to intra-patient registration. The results are discussed in Section IV, and the paper ends with some concluding remarks.

II. METHODS

The goal of our approach is to generate a statistical model of the respiratory lung motion based on a set of N_p thoracic 4D CT image sequences. Each 4D image sequence is assumed to consist of N_j 3D image volumes, which are acquired at corresponding states of the breathing cycle, e.g., maximum exhalation, mid-inhalation, maximum inhalation, mid-exhalation, and so on. This assumption is ensured by the applied 4D CT reconstruction method (see Section II-A).

The 4D mean motion model is generated in three steps (see Fig. 1).

- Step I: Estimation of the subject-specific motion for each 4D image sequence by registering the 3D image frames.
- Step II: Building an average shape and intensity atlas of the lung for a reference breathing state.
- Step III: Registration of all subject-specific motion models to the anatomical average shape and intensity atlas and generation of a mean inter-subject model of respiratory motion.

Image registration is required in all three steps. We use a non-linear, intensity-based, diffeomorphic registration method as described in Section II-B. Section II-C presents the framework for computing statistics on diffeomorphisms. The three steps to generate a statistical model of the respiratory motion are detailed in Sections II-D–II-F. The utilization of the 4D-MMM and methods to evaluate the model are presented in Section II-G and II-H.

A. 4D Image Acquisition and Image Reconstruction

4D CT images were acquired for the investigation of lung tumor mobility using a 16-slice CT scanner operated in cine-mode. During the acquisition process, the patients were instructed to breathe naturally. Between 16 and 19 couch positions per patient were investigated to ensure a complete coverage of the thorax. For each couch position, 25 scans were acquired continuously in time and synchronized spirometry measurements were recorded to associate each CT scan (i.e., 16 2D CT slices)

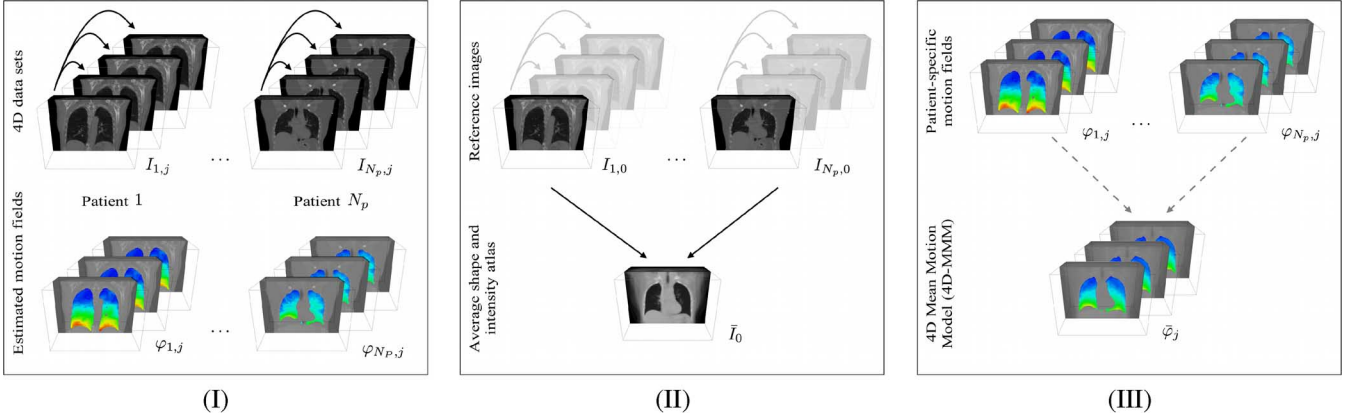


Fig. 1. Overview of the generation of the 4D-MMM: (I) First, the subject-specific motion is estimated for each 4D image sequence by registering the 3D image frames. (II) In a second step, a 3D average shape and intensity model is generated from the reference frames of the 4D CT image sequences. (III) In the last step, the average shape and intensity model is used as an anatomical reference frame to match all subject-specific motion models and to build an average inter-subject model of the respiratory motion.

with tidal volume and breathing phase (inhalation or exhalation). For further details on data acquisition see [23] and [24].

The resulting spatiotemporal series of CT scans were used to retrospectively reconstruct 4D CT data sets. A reconstructed 4D CT image data set consists of a series of 3D CT data sets reconstructed at different breathing phases that sample the patient's breathing cycle equidistantly in time. For each selected breathing phase, a tidal volume is computed based on the patient-specific spirometry records. However, free breathing causes the problem that there are often no CT scans acquired exactly at the tidal volume desired. Therefore, an optical flow based reconstruction method for 4D data sets was applied [25]. Here, a temporal interpolation scheme was derived from the optical flow equation [26] and the reconstruction method generates interpolated CT scans for exactly the predefined respiratory state. The main advantage of this method is that the 3D images can be reconstructed to arbitrary phases of the breathing cycle while the motion artifacts are minimized simultaneously. For further details and an evaluation of the reconstruction method, we refer to [25].

The reconstructed 4D image sequence for a patient p consists of N_j 3D images $I_{p,j} : \Omega \rightarrow \mathbb{R}, (\Omega \subset \mathbb{R}^3)$, reconstructed at predefined respiratory phases $j = 0, \dots, N_j - 1$. Due to the applied 4D image reconstruction method, for all patients the phases j correspond to each other. Therefore, in contrast to the work presented in [15], [17], and [27], a temporal alignment of the patient data sets is not required.

B. Diffeomorphic Image Registration

A diffeomorphic transformation $\varphi : \Omega \rightarrow \Omega$, $\Omega \subset \mathbb{R}^d$ is a globally one-to-one and differentiable mapping with a differentiable inverse, so that the topology of the structures is maintained. Constraining the transformations to be diffeomorphisms is a natural choice in medical image registration as the smoothness of anatomical features is preserved and connected structures remain connected [21]. In computational anatomy, diffeomorphic transformations are used to allow for the study of correspondences between structures of different subjects, and therefore to analyze and characterize the biological variability

of human anatomy. Diffeomorphic transformations can be modeled as arising from an evolution over unit time $t \in [0, 1]$, corresponding to the transport equations from continuum mechanics [28]. If $\mathbf{v} : \Omega \times [0, 1] \rightarrow \mathbb{R}^d$ is a time-dependent velocity field, then the diffeomorphism is initialized with the identity transform and evolves by

$$\frac{\partial}{\partial t} \phi(\mathbf{x}, t) = \mathbf{v}(\phi(\mathbf{x}, t), t), \quad \phi(\mathbf{x}, 0) = \mathbf{x}.$$

This term has a physical interpretation: if $\phi(\mathbf{x}, t) = \mathbf{y}$, then a particle placed at \mathbf{x} at time 0 ends at \mathbf{y} at time t subject to the vector field \mathbf{v} , which represents the time and position dependent velocity of this particle. Throughout this paper, $\varphi(\mathbf{x}) = \phi(\mathbf{x}, 1)$ denotes the diffeomorphic transformation we search for, i.e., the solution of the transport equation at time $t = 1$. In medical image registration applications, this characterization of diffeomorphic transformations results in time and memory consuming algorithms, because the optimization is performed on the space of time-dependent vector field flows [21].

In recent works [20], [29], diffeomorphisms are parameterized by *stationary* vector fields $\mathbf{v}(\mathbf{x}, t) = \mathbf{v}(\mathbf{x})$, i.e., the velocity fields remain constant over time. This approach still results in deformations that are diffeomorphic and has the advantage over the nonstationary setting that the resulting deformations can be computed rapidly and memory efficiently. A disadvantage of this approach is the missing physical interpretation of the velocity field. During the propagation of the deformation, each position in the stationary velocity field corresponds to different particles at different times. Furthermore, these diffeomorphisms have fewer degrees of freedom than the general case with time-dependent vector fields. In fact, only a subgroup of diffeomorphisms can be parametrized in this way. However, diffeomorphisms parameterized by stationary vector fields have been shown to be versatile enough to describe the anatomical variability in different applications [19], [29], [30].

In the perfect case (i.e., infinitely differentiable), diffeomorphisms $\varphi : \Omega \rightarrow \Omega$ form a Lie group $(\text{Diff}(\Omega), \circ)$ with the composition operation \circ , as they satisfy the requirements of closure, associativity, existence of inverse and identity. To any Lie group a Lie algebra \mathfrak{g} can be associated, which captures the local structure of $\text{Diff}(\Omega)$. The underlying vector space of \mathfrak{g} is the

tangent space $\mathcal{T}_{\text{Id}}\text{Diff}(\Omega)$ of $\text{Diff}(\Omega)$ at the neutral element Id (identity). Lie algebra and Lie group are connected by the group exponential map, which is obtained by *exponentiating* elements of the Lie algebra to produce members of the Lie group. Interestingly, for the infinite-dimensional group of diffeomorphisms, the group exponential map of a velocity field $\mathbf{v} \in \mathcal{T}_{\text{Id}}\text{Diff}(\Omega)$ corresponds to the one-parameter subgroups defined by the flow of a *stationary* vector field (see [18], [31] for a derivation)

$$\frac{\partial}{\partial t}\phi(\mathbf{x}, t) = \mathbf{v}(\phi(\mathbf{x}, t)), \text{ and } \phi(\mathbf{x}, 0) = \mathbf{x}. \quad (1)$$

The group exponential map is then defined as

$$\exp : \mathcal{T}_{\text{Id}}\text{Diff}(\Omega) \rightarrow \text{Diff}(\Omega), \exp(t\mathbf{v}(\mathbf{x})) = \phi(\mathbf{x}, t).$$

The diffeomorphism, given by the solution at $t = 1$ of (1) is given by $\varphi(\mathbf{x}) = \phi(\mathbf{x}, 1) = \exp(\mathbf{v}(\mathbf{x}))$ and can be efficiently computed with the scaling and squaring approach [20]. This efficient algorithm can be derived from the properties of the exponential map: $\exp(\mathbf{v}) = \exp((1)/(k)\mathbf{v})^k$ for $k \in \mathbb{Z}$ and is summarized in algorithm 1. Furthermore, the inverse of $\varphi(\mathbf{x})$ is defined by the exponential of the negative velocity $\varphi^{-1}(\mathbf{x}) = \exp(-\mathbf{v}(\mathbf{x}))$ and can be computed in the same way.

Algorithm 1 Computation of vector field exponentials (Scaling and Squaring)

Choose N so that $2^{-N}\mathbf{v}$ is close enough to 0, e.g., $\max \|2^{-N}\mathbf{v}(\mathbf{x})\| < (\text{voxelsize})/(2)$.
Perform an initial scaling, let $\varphi(\mathbf{x}) \leftarrow \mathbf{x} + 2^{-N}\mathbf{v}(\mathbf{x})$.
Do N recursive squarings $\varphi(\mathbf{x}) \leftarrow (\varphi \circ \varphi)(\mathbf{x})$.

It should be noted, that there are some theoretical problems yet to be solved. For example, we do not have an actual Lie group but only a pseudo-group for the infinite dimensional space of diffeomorphisms. Furthermore, the group exponential mapping is not surjective, i.e., there are elements of the group of diffeomorphisms infinitesimally close to the identity that cannot be generated by (1). However, the parametrization with stationary velocity fields leads to a very efficient implementation for diffeomorphic image registration (see below), which showed a similar registration performance (accuracy and smoothness) as diffeomorphisms parameterized by non-stationary vector fields, with a significant benefit regarding computational complexity [30].

The generation of the motion model requires the computation of numerous diffeomorphic transformations. Therefore, an efficient registration algorithm is essential in our application. Our partial differential equation (PDE) driven diffeomorphic registration framework is based on a symmetric intensity-based registration algorithm recently proposed by Vercauteren *et al.* [32]. To assure source to target symmetry, the problem of image registration between a reference image I_0 and the target image I_j is phrased as finding a diffeomorphic transformation $\varphi = \exp(\mathbf{v})$ that minimizes an energy functional¹

$$\mathcal{J}[\mathbf{v}] = \frac{1}{2}(\mathcal{D}[I_0, I_j \circ \varphi] + \mathcal{D}[I_j, I_0 \circ \varphi^{-1}]) + \alpha \mathcal{S}[\mathbf{v}]$$

¹Note that the dependence of I_j , I_0 , φ , \mathbf{v} , etc., on \mathbf{x} is assumed for the rest of the paper and may be omitted, i.e., $\varphi = \exp(\mathbf{v})$ means $\varphi(\mathbf{x}) = \exp(\mathbf{v}(\mathbf{x}))$.

where \mathcal{D} is an image distance, e.g., the sum of squared differences (SSD), and \mathcal{S} ensures the desired smoothness of the transformation [33]. The Euler–Lagrange equation associated with the minimization of the energy functional leads to the necessary condition

$$\forall \mathbf{x} \in \Omega : \quad (\text{with } \varphi = \exp(\mathbf{v})) \\ \frac{1}{2}(\mathbf{f}_{I_0, I_j \circ \varphi}(\mathbf{x}) - \mathbf{f}_{I_j, I_0 \circ \varphi^{-1}}(\mathbf{x})) + \alpha \mathcal{A}[\mathbf{v}](\mathbf{x}) = 0 \quad (2)$$

where the partial differential operator \mathcal{A} is related to the smoother \mathcal{S} and the force term \mathbf{f} is related to \mathcal{D} . We choose the diffusive smoother $\mathcal{S}[\mathbf{v}] = \int_{\Omega} \sum_{l=1}^d \|\nabla v_l\|^2 d\mathbf{x}$ with the resulting linear operator $\mathcal{A} = \Delta$, with $\mathbf{v} = (v_1, \dots, v_d)$ and Δ denotes the Laplace operator. Instead of using a force term derived from the standard SSD, \mathbf{f} is chosen to be

$$\mathbf{f}_{I_0, I_j \circ \varphi} = -\frac{(I_0 - (I_j \circ \varphi))\nabla(I_j \circ \varphi)}{\|\nabla(I_j \circ \varphi)\|^2 + \kappa^2(I_0 - (I_j \circ \varphi))^2} \quad (3)$$

with κ^2 being the reciprocal of the mean squared spacing. This force term is widely used in medical image registration [6], [34], [35] and has the advantage of generating relatively stronger forces at weak edges compared to the standard SSD. In our experience, this leads to better registration results in low contrast areas of the lung. However, at least to our knowledge there is no associated distance \mathcal{D} known and the resulting registration method can be classified as iconic feature based registration according to [35].

The resulting PDE can be used to find local minima of the associated energy functional in an iterative manner. We employ the following semi-implicit iterative scheme that can be efficiently implemented using additive operator splitting (AOS) [36] to solve (2)

$$\mathbf{v}^{k+1} = (\text{Id} - \tau\alpha\Delta)^{-1} \left(\mathbf{v}^k + \frac{\tau}{2} \left(\mathbf{f}_{I_0, I_j \circ \varphi}^k - \mathbf{f}_{I_j, I_0 \circ \varphi^{-1}}^k \right) \right)$$

where Id is the identity and τ the step length. A multiresolution scheme is used to improve registration speed and robustness. The resulting registration method is summarized in algorithm 2.

Algorithm 2 Symmetric diffeomorphic registration

Set $\mathbf{v}^0 = 0$, $\varphi = \varphi^{-1} = \text{Id}$ and $k = 0$

repeat

 Compute the forward update field

$$\mathbf{u}^{\text{forw}} = \mathbf{f}_{I_0, I_j \circ \varphi} \text{ using (3)}$$

 Compute the backward update field

$$\mathbf{u}^{\text{back}} = \mathbf{f}_{I_j, I_0 \circ \varphi^{-1}} \text{ using (3)}$$

 Calculate the next estimate of the velocity field:

$$\mathbf{v}^{k+1} = (\text{Id} - \tau\alpha\Delta)^{-1}(\mathbf{v}^k + (\tau/2)(\mathbf{u}^{\text{forw}} - \mathbf{u}^{\text{back}}))$$

 Calculate the current transformation $\varphi = \exp(\mathbf{v}^{k+1})$ and the inverse $\varphi^{-1} = \exp(-\mathbf{v}^{k+1})$

 Let $k \leftarrow k + 1$

until $\|\mathbf{v}^{k+1} - \mathbf{v}^k\| < \epsilon$ or $k \geq K_{\max}$

The reason for choosing the diffeomorphic registration approach proposed is threefold. In the context of the motion

model generation, it is important to ensure that the calculated transformations are symmetric and diffeomorphic because of the multiple usage of inverse transformations. The second reason is related to runtime and memory requirements: Due to the size of the 4D CT images diffeomorphic registration algorithms using non-stationary vector fields, e.g., [21], are not feasible. Third, the representation of diffeomorphic transformations by stationary vector fields provides a simple way for computing statistics on diffeomorphisms via vectorial statistics on the velocity fields.

C. Computing Statistics on Diffeomorphisms

In step II and step III of the model generation the computation of statistics (the mean) of (diffeomorphic) transformations is needed. Statistics of nonlinear transformations were computed before e.g., by computing the mean deformation in atlas generation methods [37], [38] or for the construction of statistical deformation models [39]. Many registration approaches use a small deformation model, in which the spatial transformation $\varphi : \Omega \rightarrow \Omega$ is parametrized by a displacement field \mathbf{u} , which is added to the identity transform: $\varphi(\mathbf{x}) = \mathbf{x} + \mathbf{u}(\mathbf{x})$. Although this additive model is applied successfully in many applications and very efficient algorithms were developed [20], this parametrization has several disadvantages. For example, the calculation of the inverse of a given transformation is expensive and the invertibility cannot be guaranteed. Furthermore, assuming a vector space with the usual additive structure leads to inconsistencies, since e.g., the inverse of $\mathbf{x} + \mathbf{u}(\mathbf{x})$ cannot be approximated by $\mathbf{x} - \mathbf{u}(\mathbf{x})$ for larger deformations (see [29] for a detailed discussion). As a consequence, this prevents the use of vectorial statistics on displacement fields, because for example the mean of a sample of invertible transformations is not necessarily invertible.

In recent years, some work has been done to define the methodology for a statistical computation framework on the manifold of diffeomorphic transformations [31], [40]. The notion of first- and second-order statistics can be extended to general metric spaces. For a general metric space \mathcal{M} with a distance $d : \mathcal{M} \times \mathcal{M} \rightarrow \mathbb{R}$, e.g., the Fréchet mean of data points x_i can be defined as the minimizer of the sum of squared distances $\bar{\mu} = \arg \min_{\mu \in \mathcal{M}} \sum_i d^2(\mu, x_i)$. Therefore, one approach is to provide the diffeomorphism group with a Riemannian metric and to define geodesic distances between diffeomorphisms [41]. Based on this distance, statistical measures like the mean can now be computed by optimization methods [38]. However, the computation of the distances and the necessary optimization results in long computational times and prevent the use of this approach in many applications.

In our application, an alternative framework to perform statistics on diffeomorphisms is used. The *Log-Euclidean* framework was introduced to compute statistics on finite-dimensional Lie groups, e.g., affine transformations or tensors. Recently, an extension of this idea to diffeomorphisms arising from (1) was presented by Arsigny *et al.* [20]. These diffeomorphisms belong to one-parameter subgroups and are parameterized by a static velocity vector field \mathbf{v} . Following [20], this parametrization is called *principal logarithm* $\mathbf{v} = \log(\varphi)$ and is a simple 3D vector field. On diffeomorphisms whose principal logarithm

is well defined, one can define a distance between diffeomorphisms $\text{dist}(\varphi_1, \varphi_2) = \|\log(\varphi_1) - \log(\varphi_2)\|$, where $\|\cdot\|$ is a norm on vector fields. This distance is a generalization of the distance defined before on the Lie group of symmetric positive-definite matrices [42]. The Log-Euclidean mean of a set of transformations φ_i is identical to the Fréchet mean related to this distance and can be computed efficiently by

$$\bar{\varphi} = \exp \left(\frac{1}{N} \sum_{i=1}^N \log(\varphi_i) \right). \quad (4)$$

The computation of the logarithm is not necessary in step II of the model generation, because $\mathbf{v} = \log(\varphi)$ is computed during the registration. In step III (Section II-F), diffeomorphic transformations are not computed directly by algorithm 2. Here, an iterative method for the estimation of the logarithm of diffeomorphisms is used [20], [43].

We chose this statistical approach in our application due to practical reasons. In contrast to the small deformation framework, the computed Log-Euclidean mean is diffeomorphic and easy to invert. Furthermore, mean and distance are inversion-invariant, since $\log(\varphi) = -\log(\varphi^{-1})$. On the other hand, there are some theoretical problems as noted in Section II-B and the metric linked to this distance is not translation invariant, since in general $\text{dist}(\varphi_1, \varphi_2) \neq \text{dist}(\varphi_1 \circ \varphi, \varphi_2 \circ \varphi)$. However, experiments show satisfying results for the generation of anatomical atlases [20] and statistics can be much more efficiently computed than in the Riemannian distance framework.

D. Step I: Intra-Patient Motion Estimation

The estimation of intra-patient respiratory motion requires the registration of 3D volumes of different respiratory states of the same patient. Let $I_{p,j} : \Omega \rightarrow \mathbb{R}$ ($\Omega \subset \mathbb{R}^3$) be the 3D volume of subject $p \in \{1, \dots, N_p\}$ acquired at respiratory state $j \in \{0, \dots, N_j - 1\}$. Without loss of generality, maximum inhale is chosen as reference breathing state and $I_{p,0}$ is the reference image of patient p . Algorithm 2 is used to compute the transformations $\varphi_{p,j} : \Omega \rightarrow \Omega$ registering the reference image $I_{p,0}$ and target images $I_{p,j}$, for all $j \in \{1, \dots, N_j - 1\}$ [see Fig. 1(I)]. Registration of 4D CT images often suffers from motion artifacts. These are reduced by the 4D CT reconstruction method applied (see Section II-A), but some residual artifacts remain. To minimize further bias on the model generation process, the regularization parameter α is chosen in such a way that the estimated motion fields do not appear to be influenced by the artifacts.

We are only interested in displacements of voxels inside the lung. Therefore, the lung needs to be segmented and segmentation masks $S_p : \Omega \rightarrow [0, 1]$ are used to restrict the registration to the lung region by computing the update field only inside the lung $\mathbf{u}(\mathbf{x}) = S_p(\mathbf{x}) \cdot \mathbf{f}_{\cdot, \cdot}(\mathbf{x})$. Beside speeding up the registration process, this approach allows us to refrain from explicitly handling the discontinuities in the respiratory motion between pleura and rib cage because moving and stationary regions of the body compete during the registration process owing to the smoothness constraint of the registration algorithm. Fig. 2 shows examples of estimated displacement fields between maximum inhale and maximum exhale.

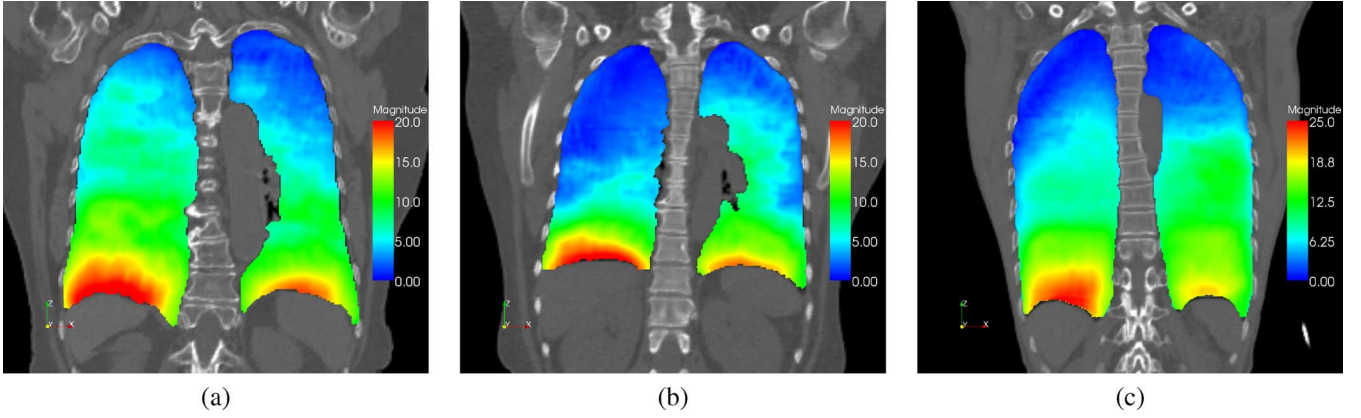


Fig. 2. Examples of computed intra-subject displacement fields. The magnitude of the estimated lung motion between end expiration and end inspiration is visualized color coded (in millimeters). The lung geometry and motion amplitude differ between patients, motion patterns appear to be similar.

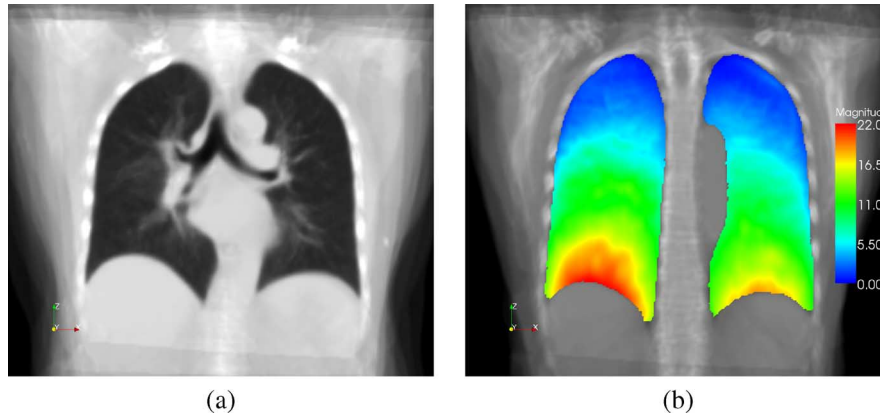


Fig. 3. Visualization of the average lung model in the state of maximum inhalation (a) and the magnitude of the mean deformation between maximum inhalation and maximum exhalation (b). In (a), the accurate registration of the lung boundary and a reasonable registration of structures inside the lung can be observed, while structures outside the lung are not matched well. The mean deformation model shows a typical respiratory motion pattern. Different windowing and leveling functions are used to accentuate inner/outer lung structures.

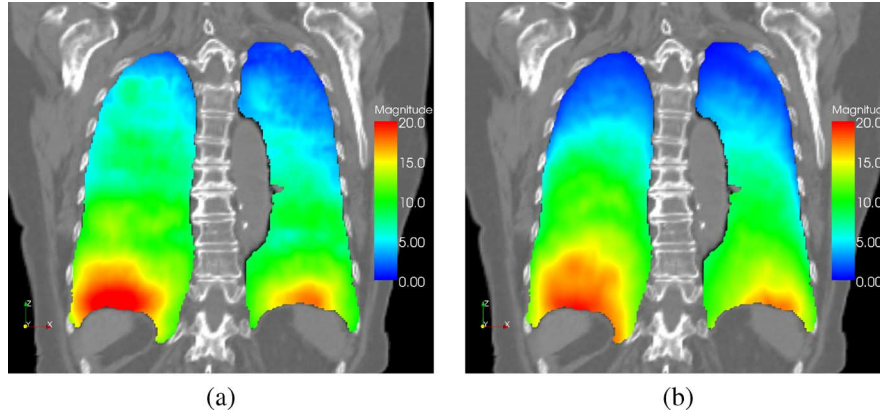


Fig. 4. Visualization of the displacement field of patient 01 estimated with nonlinear intra-patient registration (a) and the predicted displacement field using the average motion model (b). The magnitude of the displacement fields inside the lung is visualized color-coded.

Our automatic lung segmentation method follows largely [44] and consists of three steps: 1) automatic lung segmentation using thresholding and morphological operations, 2) identification and removal of the central airways, and 3) separation of the right and left lungs if needed. In contrast to the 2D morphological operation proposed in [44], Dijkstra's algorithm is used in step 3 to find an optimal separation path in CT slices where gray-scale thresholding fails to separate the left and right lungs.

E. Step II: Building the Average Shape and Intensity Atlas

The computed intra-subject models of the lung motion are used to generate an inter-subject model of respiratory motion that reflects the mean motion of all subjects. To build a statistical model of respiratory motion, correspondence between different subjects has to be established, i.e., an anatomical reference frame is necessary. The computed transformations $\varphi_{p,j}$ are

defined in the reference image $I_{p,0}$ of patient p . Therefore, the reference images $I_{p,0}$ for $p = 1, \dots, N_p$ are used to generate an average intensity and shape atlas \bar{I}_0 of the lung in the reference breathing state. This 3D lung atlas is used as reference frame for the statistical lung motion model.

In recent years, intensive research has been directed toward the development of digital 3D atlases of the human anatomy using image matching techniques. In this context, inverse consistent diffeomorphic image registration has been proved to be favorable to generate average anatomical atlases [45]. In our application, we use the symmetric diffeomorphic registration method introduced in Section II-B in combination with a statistical atlas building method proposed by Guimond *et al.* [37] to generate a 3D atlas of the lung. Our atlas generation method is summarized in algorithm 3.

Algorithm 3 Generation of an average shape and intensity atlas

Given: a set of 3D images $I_{p,0}$ ($p = 1, \dots, N_p$)

Choose an initial reference image, e.g., $\bar{I}_0^0 = I_{1,0}$, set $k = 0$

repeat

for all subjects p **do**

 Compute the transformation ψ_p to register $I_{p,0}$ and \bar{I}_0^k using an affine preregistration and algorithm 2.

end for

 Compute the inverse average transformation

$$\bar{\psi}^{-1} = \exp \left(-\frac{1}{N_p} \sum_p \log(\psi_p) \right)$$

 Generate the new average intensity and shape image

$$\bar{I}_0^{k+1}(x) = \frac{1}{N_p} \sum_p I_{p,0}(\psi_p \circ \bar{\psi}^{-1}(x))$$

$k \leftarrow k + 1$

until $\|\bar{I}_0^{k+1} - \bar{I}_0^k\| < \epsilon$ or $k > K_{\max}$

Fig. 3(a) shows the average lung image \bar{I}_0 generated with algorithm [3]. In contrast to the method proposed by Guimond *et al.*, the averaging of the transformation is performed in the Log-Euclidean space to ensure diffeomorphic transformations. Note that the velocity fields $\mathbf{w}_p = \log(\psi_p)$ are computed during the symmetric diffeomorphic registration and therefore no explicit calculation of the logarithm is necessary. The inverse average transformation $\bar{\psi}^{-1}$ is easily computed from the negative mean velocity by algorithm 1. In the implementation, transformation ψ_p is composed of a global affine transformation and a local nonlinear freeform deformation.

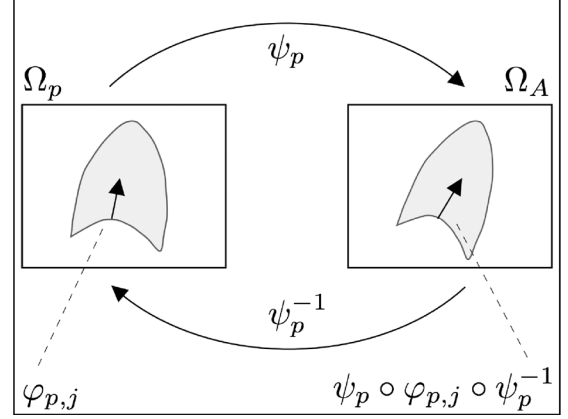


Fig. 5. The spatial transformation $\psi_p \circ \varphi_{p,j} \circ \psi_p^{-1}$ between atlas- and patient coordinate system Ω_A and Ω_p eliminates subject-specific size and orientation information in the motion fields $\varphi_{p,j}$. Such a coordinate transformation accounts for the differences in the coordinate systems of subject and atlas due to misalignment and size/shape variation and enables the quantitative and qualitative comparison of motion fields of different subjects.

F. Step III: Generation of the 4D Mean Motion Model

The intra-subject motion fields, calculated in the first step of the model generation process, are diffeomorphic mappings defined in the anatomical coordinate system of subject p : $\varphi_{p,j} : \Omega_p \rightarrow \Omega_p$. The registered images $I_{p,j}$, $j = 0, \dots, N_j - 1$ show the anatomy for subject p at different time points and the derived motion is expressed relative to the chosen reference image $I_{p,0}$. To compare the transformed fields of a number of different subjects, the intra-subject motion fields are mapped into the atlas coordinate system Ω_A . Let $\psi_p : \Omega_p \rightarrow \Omega_A$ be the transformation between the reference image $I_{p,0}$ of subject p and the atlas image \bar{I}_0 . Consider a point $x \in \Omega_A$ with the corresponding point $x' = \psi_p^{-1}(x) \in \Omega_p$, then the point $y' = \varphi_{p,j}(x')$ transformed by the motion field in Ω_p corresponds to $y = \psi_p(y') \in \Omega_A$. Thus, the transformation of the patient-specific motion field $\varphi_{p,j}$ into the atlas coordinate system is given by

$$\tilde{\varphi}_{p,j} = \psi_p \circ \varphi_{p,j} \circ \psi_p^{-1}. \quad (5)$$

In Fig. 5 a schematic sketch is shown to clarify this transformation. The coordinate transformation accounts for the differences in the coordinate systems of subject and atlas due to misalignment and size/shape variation and eliminates subject-specific size, shape and orientation information in the deformation vectors. In contrast to the method proposed in [16], the inverse transformation ψ_p^{-1} is available and no numerical approximation is needed.

In this manner, for each breathing state j the intra-patient motion models $\varphi_{p,j}$, $p = 1, \dots, N_p$ are mapped to the common coordinate space of \bar{I}_0 . The mean motion model $\bar{\varphi}_j$ is generated by calculating the Log-Euclidean mean of the mapped transformations

$$\begin{aligned} \bar{\varphi}_j &= \exp \left(\frac{1}{N_p} \sum_p \log(\tilde{\varphi}_{p,j}) \right) \\ &= \exp \left(\frac{1}{N_p} \sum_p \log(\psi_p \circ \varphi_{p,j} \circ \psi_p^{-1}) \right). \end{aligned} \quad (6)$$

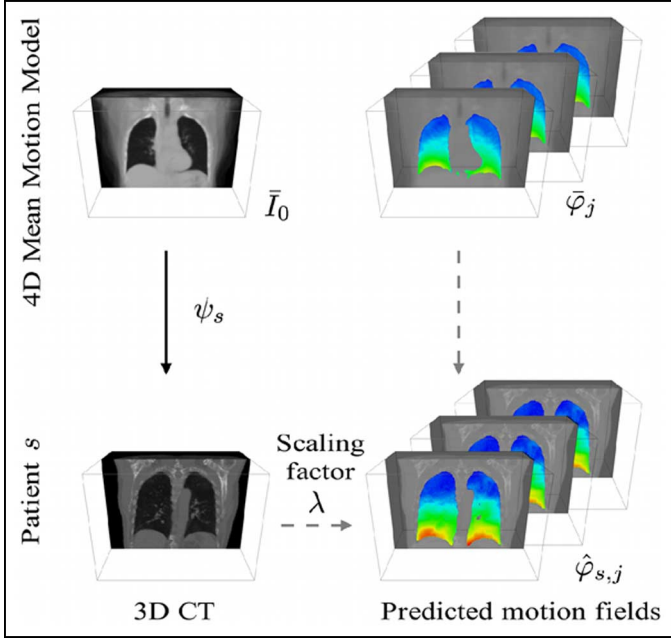


Fig. 6. Utilization of the 4D-MMM for motion prediction: the average lung atlas is registered with the 3D patient image and the resulting transformation is used to apply a coordinate transformation of the mean motion fields. The patient-specific scaling factor λ accounts for the individual amplitude of respiratory motion.

With $\varphi_{p,j} = \exp(\mathbf{v}_{p,j})$ and $\psi_p = \exp(\mathbf{w}_p)$ we could approximate $\log(\hat{\varphi}_{p,j}) = \log[\exp(\mathbf{w}_p) \circ \exp(\mathbf{v}_{p,j}) \circ \exp(-\mathbf{w}_p)]$ using the Backer–Campbell–Hausdorff formula [18]. However, the approximation error depends on the norm of the (non-small) velocity fields \mathbf{w}_p and $\mathbf{v}_{p,j}$. Therefore, we concatenate the diffeomorphic transformations $\psi_p \circ \varphi_{p,j} \circ \psi_p^{-1}$ and use the method proposed in [43] to compute the logarithm.

The resulting 4D-MMM consists of an average lung image \bar{I}_0 for a reference state of the breathing cycle, e.g., maximum inhalation, and a set of motion fields $\bar{\varphi}_j$ describing an average motion between the respiratory state j and the reference state [Fig. 3(b)]. Such a model can now be used to predict patient-specific breathing motion or to compare individual motion patterns to the mean motion.

G. Utilization of the 4D-MMM for Individual Motion Prediction

The 4D-MMM generated in Sections II-D–II-F can be used to predict respiratory lung motion of a subject s even if no 4D image information is available (see Fig. 6). Therefore, availability of a 3D image $I_{s,0}$ acquired at the selected reference state of the breathing cycle is presumed to permit the adaptation of the 4D-MMM to the individual lung geometry of subject s . In a first step, the average lung atlas \bar{I}_0 is registered with the 3D image $I_{s,0}$. The resulting transformation ψ_s is used to apply a coordinate transformation to the mean motion fields to obtain the model-based prediction of the subject-specific lung motion fields: $\hat{\varphi}_{s,j} = \psi_s^{-1} \circ \bar{\varphi}_j \circ \psi_s$.

However, two problems arise. First, breathing motion of different individuals varies significantly in amplitude [46]. Therefore, motion prediction using the mean amplitude will produce unsatisfactory results. To account for subject-specific motion

amplitudes, we propose to introduce an additional parameter λ to adapt the 4D-MMM to the individual depth of respiration. We assume that differences in the depth of breathing can be simulated by a scaling of the associated motion fields. The scaling is performed in the Log-Euclidean, i.e., by $\hat{\varphi}_{s,j}^{(\lambda)} = \exp(\lambda \hat{\mathbf{v}}_{s,j})$, to ensure that the scaled motion field is diffeomorphic. Here, the same factor is used to scale the predicted motion fields for all breathing phases. This means the variability of the breathing motion is expressed by a single parameter in our model, which could be described as “depth of respiration.” This is a simplifying assumption since, e.g., chest and abdominal breathing cannot be described in this way. However, we will evaluate the prediction quality of this model in Section III.

Additional information is required to determine the correct scaling factor λ for a patient. In this work, we suggest to use the total change in lung air content ΔV_{air} between end inspiration and end expiration. Even without 4D CT data, this information can be acquired by spirometry measurements, because a linear dependency between the measured tidal volume and the air content change can be assumed [24]. But in general, other measurements can also be used to calculate appropriate scaling factors, e.g., the amplitude of the diaphragm motion or the change of the lung volume.

Let end inspiration (EI) be the reference breathing state and the predicted motion field between end expiration (EE) and end inspiration $\hat{\varphi}_{s,\text{EE}}$ be given. The velocity field $\hat{\mathbf{v}}_{s,\text{EE}} = \log(\hat{\varphi}_{s,\text{EE}})$ is computed once by an iterative scheme (see Section II-C). Given $\hat{\mathbf{v}}_{s,\text{EE}}$, the inverse transformation $\hat{\varphi}_{s,\text{EE}}^{(-\lambda)} = \exp(-\lambda \hat{\mathbf{v}}_{s,\text{EE}})$ can easily be computed (alg. 1) and used to deform $I_{s,\text{EI}}$ towards end expiration: $I_{s,\text{EE}} \approx I_{s,\text{EI}} \circ \hat{\varphi}_{s,\text{EE}}^{(-\lambda)}$. We then search a scaling factor λ so that the difference in the air contents is close to ΔV_{air} : $\lambda = \arg \min_{\lambda} |(V_{\text{air}}(I_{s,\text{EI}}) - V_{\text{air}}(I_{s,\text{EI}} \circ \hat{\varphi}_{s,\text{EE}}^{(-\lambda)})) - \Delta V_{\text{air}}|$.

The air content of the reference image is computed using the method described in [24]. The Hounsfield unit (HU) of a lung voxel is primarily contributed by tissue (parenchyma, blood), with approximately 55 HU, and air with -1000 HU, and the air volume of each voxel is computed by $V_{\text{air}}(\mathbf{x}) = v(\mathbf{x})(1 - (1000 + I_{s,\text{EI}}(\mathbf{x})/1000 + 55))$, where $v(\mathbf{x})$ is the voxel volume.

As pointed out before by Sarrut *et al.* [6] and Yin *et al.* [47], a deformation of image $I_{s,\text{EI}}$ does not change voxel intensities as it would be appropriate due to changes in lung densities during breathing. Assuming that the tissue mass of each lung voxel is constant during breathing, the volume change due to deformation directly increases or decreases the air volume. The air volume change of voxel \mathbf{x} due to the deformation φ can then be approximated by

$$V_{\text{air}}(\mathbf{x}; \varphi) = J(\mathbf{x}, \varphi)v(\mathbf{x}) - v(\mathbf{x}) \frac{1000 + I_{s,\text{EI}}(\mathbf{x})}{1000 + 55} \quad (7)$$

where $v(\mathbf{x})(1000 + I_{s,\text{EI}}(\mathbf{x})/1000 + 55)$ is the tissue volume (which is assumed to be constant under deformation), and $J(\mathbf{x}, \varphi)$ is the Jacobian value, i.e., the determinant of the Jacobian of the deformation field: $J(\mathbf{x}, \varphi) = \det(\nabla \varphi(\mathbf{x}))$. The Jacobian value is greater than 1 if there is local expansion and less than 1 if there is local contraction. A Jacobian value of 1 corresponds to no volume change. Because the tissue volume is

TABLE I
DATA SET CHARACTERISTICS: TIDAL VOLUME ΔV_{air} FOR LEFT AND RIGHT LUNG, TUMOR SIZE (BASED ON TUMOR SEGMENTATION AT END-EXPIRATION), AND TUMOR LOCATION FOR THE PATIENTS CONSIDERED

Data set	ΔV_{air}		Tumor size	Tumor location
	Left	Right		
Patient 01	171 ml	193 ml	6.5 cm ³	right lower lobe
Patient 02	338 ml	211 ml	7.6 cm ³	right upper lobe (adhering to cranial tip of the lung) (emphysema in both lungs)
Patient 03	177 ml	176 ml	12.7 cm ³	left upper lobe (adhering to anterior chest wall)
Patient 04	167 ml	211 ml	—	left lower lobe, but no solid tumor
Patient 05	234 ml	165 ml	8.2 cm ³	right upper lobe (adhering to posterior chest wall)
Patient 06	304 ml	411 ml	17.3 cm ³	right upper lobe (adhering to right hilum)
			3.4 cm ³	left lingula
			128.2 cm ³	close to right hilum (adhering to posterior chest wall)
Patient 07	365 ml	416 ml	2.8 cm ³	right upper lobe (near cranial tip of the lung)
Patient 08	242 ml	256 ml	18.4 cm ³	close to right hilum
Patient 09	251 ml	264 ml	88.9 cm ³	right upper lobe (adhering to right hilum)
Patient 10	189 ml	260 ml	96.1 cm ³	right middle lobe (adhering to posterior chest wall)
Patient 11 – 17 suffer from abdominal tumors (pancreas, spleen) and are not used for the evaluation, but for model generation only.				

independent of φ in (7), the average Jacobian value $\bar{J}(\varphi)$ and the total volume V of all lung voxels with $I_{s,\text{EI}}(\mathbf{x}) < -250$ HU is computed and $|(1 - \bar{J}(\hat{\varphi}_{s,\text{EE}}^\lambda)) \cdot V - \Delta V_{\text{air}}|$ is minimized to find the optimal scaling factor λ . The threshold of -250 HU is chosen to exclude large vessels from the Jacobian computation. Breathing-related variations of the mass of the pulmonary parenchyma due to the distension of blood vessels, and due to the changing perfusion were reported in [4]. The variations of tissue mass are neglected by the assumption of a constant tissue volume. However, the variations are reported to be $<10\%$ and the influence on the scaling factor should be small.

Beside the determination of the scaling factor, a second problem arises when predicting individual breathing motion of lung cancer patients. Lung tumors will impair the atlas-patient registration because there is no corresponding structure in the atlas. This leads to distortions in ψ_s near the tumor region and consequently the predicted motion fields $\hat{\varphi}_{s,j}$ are affected. Therefore, we decided to compute ψ_s by registering lung segmentation masks from atlas and subject s and by omitting the inner lung structures. In a first step, an affine alignment of the lung surfaces is computed by the iterative-closest-point algorithm [48]. Then, smoothed lung segmentation images are matched by the diffeomorphic intensity-based registration (Algorithm 2).

H. Evaluation Methods

Based on static 3D images of test cases, the generated 4D-MMM is used to predict individual breathing motion without 4D image information as described in the last section. The model-based prediction of the lung motion $\hat{\varphi}_{s,j}$ is compared to the individual motion fields $\varphi_{s,j}$ extracted from 4D CT images by intra-patient registration. Note that $\hat{\varphi}_{s,j}$ is estimated without 4D image information about this subject, whereas $\varphi_{s,j}$ relies on patient-specific 4D images.

To perform a quantitative evaluation of both methods, anatomical landmarks in the lung are identified by medical experts in all phases of the breathing cycle and the target registration errors are determined. For a given motion field φ_j , the target registration error $R_j^k = \|\Delta \mathbf{l}_j^{k,\text{predict}} - \Delta \mathbf{l}_j^{k,\text{actual}}\|$ is the difference between the motion of landmark k estimated by φ_j and the landmark motion as observed by the medical

expert, where $\Delta \mathbf{l}_j^{k,\text{actual}} = \mathbf{l}^k(I_{s,0}) - \mathbf{l}^k(I_{s,j})$, $\Delta \mathbf{l}_j^{k,\text{predict}} = \varphi_j(\mathbf{l}^k(I_{s,j})) - \mathbf{l}^k(I_{s,j})$, and $\mathbf{l}^k(I)$ denotes the position of landmark k in image I as identified by the medical expert.

A second evaluation procedure is related to an application in radiotherapy. Based on expert-defined tumor segmentations, the performance of the model-based motion prediction is assessed. This aims to answer the question whether or not the model-based motion field estimation provides a good prediction of lung tumor motion, although the motion modeling focuses on the representation of “healthy” lung dynamics and therefore motions impaired by tumors or other lung diseases are not included in the model. In this evaluation study, the distances of the mass centers between a manual tumor segmentation in the reference image and the transformed tumor segmentation of the target image are used to quantify the accuracy of the predicted tumor motion.

III. RESULTS

To capture the respiratory motion of the lung, 4D CT image sequences were acquired from 10 lung cancer patients and seven patients with abdominal tumors outside the lungs during free breathing using the scanning protocol and reconstruction method described in Section II-A. The spatial resolution of the reconstructed 4D CT data sets is between $0.78 \times 0.78 \times 1.5$ mm³ and $0.98 \times 0.98 \times 1.5$ mm³. Each data set consists of 3D CT images at 10 to 14 preselected breathing phases. In this study, we use the following 4 phases of the breathing cycle: end inspiration (EI) (used as reference phase), 42% exhale (ME), end expiration (EE), and 42% inhale (MI). Due to memory and computation time restrictions, the 3D volumes were down-sampled to a spatial resolution of $320 \times 320 \times 220$ voxels with $1.5 \times 1.5 \times 1.5$ mm³. A clinical expert delineated left and right lung and the lung tumors in the images. Characteristics (tidal volume, tumor size, tumor location) of the acquired patient data are shown in Table I.

The 4D images of patients 01 to 10 are used for the quantitative evaluation. Between 70 and 90 inner lung landmarks (prominent bifurcations of the bronchial tree and the vessel tree) were identified in each of the four 3D CT images for these patients, about 3200 landmarks in total. Landmark identification was repeated to assess the intraobserver variability. The

TABLE II
LANDMARK MOTION AMPLITUDES $\|\Delta t_{EE}^{k,actual}\|$, MAGNITUDE OF THE INTRAOBSERVER VARIABILITY (IO) OF LANDMARK IDENTIFICATION, AND TARGET REGISTRATION ERROR \bar{R}_{EE} FOR THE PATIENTS CONSIDERED. VALUES ARE AVERAGED OVER ALL LANDMARKS PER PATIENT. LUNGS WITH IMPAIRED MOTION ARE INDICATED BY A GRAY TEXT COLOR

Data set	Lung	Landmark motion [mm]		Target registration error \bar{R}_{EE} [mm]	
		$\ \Delta t_{EE}^{k,actual}\ $	IO	Intra-patient registration	Model-based prediction
Patient 01	left	4.99 \pm 4.84	0.9 \pm 0.7	1.51 \pm 1.31	2.40 \pm 1.35
	right	7.25 \pm 4.47		1.41 \pm 0.83	3.99 \pm 2.07
Patient 02	left	7.09 \pm 2.92	1.0 \pm 0.9	2.28 \pm 1.73	4.29 \pm 1.26
	right	4.21 \pm 1.75		1.16 \pm 0.61	3.82 \pm 1.10
Patient 03	left	6.15 \pm 2.26	0.9 \pm 0.8	1.38 \pm 0.73	3.68 \pm 1.31
	right	6.28 \pm 2.01		1.78 \pm 1.05	3.65 \pm 1.38
Patient 04	left	6.65 \pm 2.56	1.0 \pm 0.7	1.53 \pm 0.93	4.01 \pm 1.59
	right	6.22 \pm 3.52		1.44 \pm 0.82	2.20 \pm 1.09
Patient 05	left	5.77 \pm 2.03	1.0 \pm 0.8	1.50 \pm 0.80	3.17 \pm 1.34
	right	3.18 \pm 3.36		1.29 \pm 1.04	3.41 \pm 1.97
Patient 06	left	9.67 \pm 8.32	0.8 \pm 0.9	1.64 \pm 1.42	5.78 \pm 2.35
	right	11.85 \pm 7.08		1.60 \pm 1.00	4.69 \pm 1.90
Patient 07	left	8.22 \pm 6.52	1.1 \pm 0.8	2.45 \pm 2.22	4.02 \pm 1.57
	right	4.99 \pm 6.65		1.49 \pm 1.48	3.35 \pm 1.69
Patient 08	left	5.78 \pm 4.14	0.9 \pm 0.8	1.18 \pm 0.57	3.15 \pm 1.70
	right	6.28 \pm 5.63		1.25 \pm 1.03	3.05 \pm 2.30
Patient 09	left	7.43 \pm 5.34	0.9 \pm 0.8	1.42 \pm 1.22	2.75 \pm 1.40
	right	8.41 \pm 5.22		1.67 \pm 1.03	3.34 \pm 2.07
Patient 10	left	7.63 \pm 5.83	0.8 \pm 0.9	1.93 \pm 2.10	3.15 \pm 2.18
	right	8.85 \pm 6.76		1.76 \pm 1.33	5.08 \pm 2.35

mean landmark motion magnitude, i.e., the mean distance of corresponding landmarks, between EI and EE is 6.8 ± 5.4 mm, (2.6 ± 1.6 mm between EI and ME and 5.0 ± 2.8 mm between EI and MI). The intraobserver variability is 0.9 ± 0.8 mm (determined in the CT data of full resolution).

A. Model Generation

In the first step, we compute the patient-specific motion fields $\varphi_{p,j}$ describing the lung motion from maximum inhale (reference) to the other three breathing states using the algorithm described in Section II-D. The registration parameters were determined empirically on a set of test data sets. A multi-resolution strategy with four levels was used in all registration steps. The regularization parameter $\alpha = 1.0$ was chosen by comparing the TRE of manually placed landmarks and a visual inspection of the alignment of lung boundaries and vessel structures for several values of α . A reasonable choice for the stepwidth is $\tau = 1.0$, which provides fast enough convergence while maintaining stability. The latter is explained by the chosen force term (3), which restricts the maximal magnitude of the force vectors to half of the mean voxel spacing.

Resulting motion field estimates are visualized in Fig. 2. The TRE of the intra-patient registration is a lower bound for the accuracy of the model-based prediction using the 4D-MMM. The average TRE \bar{R}_{EE} between the reference phase (EI) and EE for patients 01–10 (averaged over all landmarks and patients) is 1.6 ± 1.3 mm. Details for all test data sets are shown in Table II. The average registration residual for ME and MI is also in the range of the voxel size (see Table III).

The estimated motion fields are used to generate a statistical model of the respiratory motion as described in Section II-E. The resulting model consists of the average lung image \bar{I}_{EI} and the motion fields $\bar{\varphi}_{EE}$, $\bar{\varphi}_{ME}$, and $\bar{\varphi}_{MI}$ describing the mean motion between the respiratory states EE, ME, MI, and the reference phase EI.

TABLE III
LANDMARK MOTION AMPLITUDES $\|\Delta t_j^{k,actual}\|$ AND AVERAGED TARGET REGISTRATION ERROR \bar{R}_j BETWEEN THE REFERENCE BREATHING PHASE (EI) AND EE, ME, AND MI. VALUES ARE AVERAGED OVER ALL LANDMARKS AND ALL PATIENTS

breathing phase j	Landmark motion [mm] $\ \Delta t_j^{k,actual}\ $	Target registration error \bar{R}_j [mm]		
		intra-patient registration	Model-based prediction intact lungs	impaired lungs
<i>EI</i> \rightarrow <i>EE</i>	6.8 \pm 5.4	1.6 \pm 1.3	3.3 \pm 1.6	4.0 \pm 2.0
<i>EI</i> \rightarrow <i>ME</i>	2.6 \pm 1.6	1.5 \pm 0.8	1.8 \pm 1.0	2.3 \pm 1.2
<i>EI</i> \rightarrow <i>MI</i>	5.0 \pm 2.8	1.6 \pm 0.9	2.7 \pm 1.3	3.3 \pm 1.6

The aim of the model generation is to create a representation of the mean healthy lung motion. In a dynamic MRI study by Plathow *et al.* [49], tumors with diameter > 3 cm were shown to influence respiratory lung dynamics. According to their observations, we divide the lungs into two groups: lungs with *intact* dynamics and lungs with *impaired* motion. Lungs without or with only small tumors (tumor volume < 14.1 cm³, which corresponds to a spherical tumor with a diameter $\varnothing < 3$ cm) are defined as intact. Lungs with large tumors ($\varnothing > 3$ cm) or lungs affected by other diseases (e.g., emphysema) are defined as impaired. To prevent bias by pathological images we use data sets of only intact lungs to generate the average shape and intensity image \bar{I}_{EI} . To increase the number of available samples for statistics, right and left lung are considered separately for computation of the mean motion model. Impaired lung sides are excluded from the mean motion computation. Sixteen data sets remain for the model generation of the left lung and 11 data sets for the right lung. In Fig. 3(a), a slice of the constructed average shape and intensity image \bar{I}_{EI} is shown. An accurate registration of the lung boundary and a good registration of structures inside the lung can be observed. Structures outside the lung are not matched well because the registration is restricted to the lung region. The magnitude of the displacement between maximum

TABLE IV
TUMOR MOTION AMPLITUDE AND THE CENTER DISTANCES BETWEEN MANUAL SEGMENTED TUMOR AND PREDICTED TUMOR POSITION BETWEEN EE AND EI IN [MM] (SEE TEXT FOR DETAILS)

Data set	lung	Tumor motion	Center distances		large	adherent
			Intra-patient registration	Model-based prediction		
Patient 01	right	12.20	0.45	3.35		
Patient 02	right	2.15	1.44	3.90		X
Patient 03	left	6.74	0.41	3.91		X
Patient 05	right	2.34	1.95	5.53		X
Patient 06	right	1.68	1.05	4.71	X	X
	left	19.78	2.12	6.49		
	right	13.78	0.97	2.85	X	
Patient 07	right	1.31	0.42	0.66		
Patient 08	right	6.24	0.90	2.00	X	
Patient 09	right	8.35	0.29	3.18	X	X
Patient 10	right	1.77	1.01	7.38	X	X

inhale and maximum exhale of the mean motion model is visualized for the left and right lung in Fig. 3(b). A smooth transition from large motion amplitudes near the diaphragm to small motion amplitudes near the tip of the lung is visible.

B. Landmark-Based Evaluation of Lung Motion Prediction

In a first quantitative evaluation, the target registration errors R of the model-based motion prediction are computed for the ten test data sets. All of them were acquired from lung cancer patients (see Table I). To be able to provide results of the model-based prediction for healthy and impaired lungs, left and right lungs are handled separately during the evaluation. For each test data set, the 4D-MMM is transformed into the subject's coordinate space and used to predict landmark motion. A leave-one-out strategy is applied to ensure that the individual patient data is not used for the model generation. The change in lung air content ΔV_{air} needed for the computation of the scaling factor λ was calculated from the CT images I_{EI} and I_{EE} for each lung side and each test data set. The same factor λ was used to scale the predicted motion fields $\hat{\varphi}_{\text{EE}}$, $\hat{\varphi}_{\text{ME}}$, and $\hat{\varphi}_{\text{MI}}$. Besides ΔV_{air} , no 4D information is used for the model-based prediction. Fig. 4 shows the motion field predicted by the 4D-MMM and the motion field computed by patient-specific registration for patient 01. Qualitatively, a good correspondence between the two motion fields is visible, except in the right upper lobe, where small deviations occur.

The average target registration errors \bar{R}_{EE} are listed in Table II for each of the test data sets and for both patient-specific and model-based motion estimation. Lungs with impaired motion are indicated by a gray text color. Regarding Table II, lungs with impaired motion generally show higher target registration errors for the model-based prediction than intact lungs. An exception constitutes the left lung of patient 06, where the highest target registration error occurs. The inspection of an expert led to the conclusion that a strong compensatory motion exists due to the large tumor in the right lung. In order to assess the results for all three breathing phases EE, ME and MI the mean landmark motion and the mean target registration errors of the intra-patient registration are compared to the model-based prediction quality. The results are given in Table III, where the values of the model-based prediction are given separately for intact and impaired lungs. The average TRE \bar{R}_{EE} for intact

lungs is 3.3 ± 1.6 mm, which is significantly lower ($p < 0.05$) than for lungs with impaired motion ($\bar{R}_{\text{EE}} = 4.0 \pm 2.0$ mm). Significance is tested by applying a multilevel hierarchical model with the individual R^k values nested within the patient (software: SPSS v.17); data are logarithmized to ensure normal distribution and the model is adjusted to landmark motion.

C. Model-Based Prediction of Tumor Motion

For a second evaluation of the model, we use expert generated tumor segmentations in two breathing phases (maximum inhale and maximum exhale) of nine patient data sets. Patient 04 is excluded because no solid tumor could be delineated. The 4D-MMM is transformed into the coordinate space of each test data set (see Section II-G) and then used to warp the expert generated tumor segmentation at maximum exhale towards maximum inhale. To evaluate the accuracy of the model-based prediction, the distances of the mass centers of tumor segmentations were calculated: 1) between the unregistered inhale and exhale expert segmentation images (tumor motion amplitude), 2) between the inhale segmentation and the exhale segmentation warped by the deformation field obtained by the intra-patient registration, and 3) between the inhale segmentation and the exhale segmentation warped by the 4D-MMM.

Corresponding results are summarized in Table IV. Large tumors with a diameter > 3 cm influence respiratory lung dynamics and are marked in the table as large. Furthermore, it has turned out that the model-based prediction of the tumor motion is degraded if the tumor adheres to a non-lung structure. In these cases, the model presumes that the tumor moves like surrounding lung tissue, whereas, it rather moves like the adjacent non-lung structure (e.g., chest wall or hilum). The last column in Table IV marks those tumors. The model-based predicted motion of the tumor mass center from EI to EE ranges from 0.66 to 7.38 mm. There is no significant correlation between the tumor motion amplitude and the accuracy of the model-based predicted mass center ($r = 0.19$, $p = 0.15$). Furthermore, it cannot be shown that the prediction accuracy for small tumors is significantly better than for large tumors ($p = 0.4$). However, the model-based prediction accuracy of non-adherent tumors is significantly better than for tumors adhering to chest wall or hilum ($p < 0.05$). Significance is tested by applying a linear mixed model (software: SPSS v.17) and the model is adjusted to tumor motion.

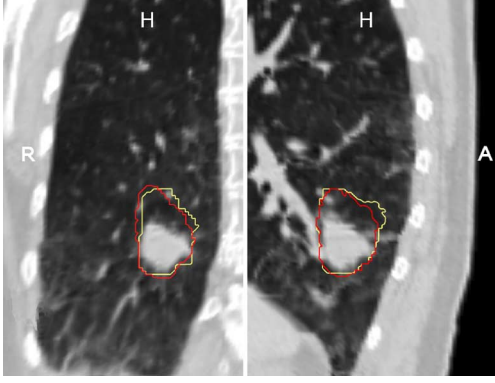


Fig. 7. Visualization of the internal target volume (ITV) of patient 01 in a coronal (left) and sagittal (right) CT slice. The ITV was calculated from expert-defined tumor segmentations in EI, EE, ME, and MI (yellow contour) and from tumor positions predicted by the average motion model (red contour).

D. Application Examples

The capability of the 4D-MMM to predict tumor motions for radiotherapy planning is exemplarily illustrated for patient 01. As shown in Sections III-B and III-C, model-based prediction accuracy is decreased for large tumors and tumors adhering to non-lung structures, and the model cannot be applied in these cases. Patient 01 shows a small tumor not adherent to another structure, and a therapeutic relevant tumor motion of 12.2 mm (respiratory motion management is appropriate when target motion is > 5 mm [1]). The prediction accuracy of the tumor motion from EI to EE of 3.54 mm is near the landmark-based average registration residual of intact lungs. The internal target volume (ITV) in 3D conformal radiotherapy contains the complete range of motion of the tumor [50]. For this patient, the ITV is first calculated from expert-defined tumor segmentations in the images acquired at EI, EE, ME, and MI. In a second step, the expert segmentation in EI is warped to EE, ME and MI using the 4D-MMM and the ITV is calculated based on the warped results. The outlines of both ITVs are shown in Fig. 7. Please note that beside the calculated scaling factor λ no patient-specific motion information is used for the model-based prediction.

A second example demonstrates that the 4D-MMM could be helpful from the perspective of image-guided diagnosis. Here, the motion pattern of individual patients are compared to a “normal” motion, represented by the mean motion model. In Fig. 8, the magnitude of the difference between the individual motion field φ_{EE} computed by intra-patient registration and the model-based predicted motion field $\hat{\varphi}_{EE}$ is shown for patient 10. The left lung shows differences of about 3 mm, whereas the large differences to the intact lung motion indicate that the respiratory dynamics of the right lung are influenced by the large tumor. Very high differences are visible near the tumor, because the tumor is adhering to the posterior chest wall and does not follow the lung motion.

IV. DISCUSSION AND CONCLUSION

In this paper, we addressed the problem of extracting, modeling and predicting respiratory motion. We proposed a method to generate an inter-subject statistical model of the breathing motion, based on individual motion fields extracted from 4D

CT images of 17 patients. Methods for using this model to predict patient-specific breathing motion without knowledge of 4D image information were presented. Ten 4D CT data sets were used to evaluate the accuracy of the image-based motion field extraction and the model-based motion field prediction.

A symmetric diffeomorphic nonlinear intensity-based registration method was used to extract patient-specific breathing motion. The mean error after registration (TRE) between EI and EE images was 1.6 ± 1.3 mm. Comparing these results to other studies [51], [52] and taking image resolution ($1.5 \times 1.5 \times 1.5$ mm³) into account, we consider the TRE states a lower bound of registration accuracy.

The extracted patient-specific motion fields were used to generate an inter-subject statistical model of the breathing motion. Inter-patient correspondence was established by patient-atlas registration with an average shape and intensity atlas of the lung and the Log-Euclidean framework [20] was used for the required computations of statistics on the diffeomorphic transformations. Although built on only a small patient population, the computed mean motion model presents a typical respiratory motion pattern.

The average motion model is adapted to unseen data by a registration of the model lung surface with the lung surface in the reference image of the new patient, to cope with tumors or other pathological structures. The end inspiration image is used as reference image because the total change in lung air content between end inspiration and end expiration is used as patient-specific motion indicator. Caused by our limited test data set we compute different scaling factors for left and right lungs to provide results of the model-based prediction for healthy and impaired lungs. This would obviously not be possible if the scaling factor was really calculated from spirometry and prediction quality may be influenced by this. However, these influences should be small for intact lungs. As noted in Section II-G, alternative measures can be used, e.g., the motion of the diaphragm or other anatomical landmarks, and in this case again a calculation of different scaling factors for each lung is possible. Furthermore, other breathing phases could be used as reference, e.g., some mid-ventilation images. However, taking the symmetric behavior of our registration approach into account, Table III indicates that such a change of the reference image would have only small effects on the TRE for intra-patient registration. Further, the choice of EE or EI images is favorable for inter-patient registration, since mid-ventilation images are more affected by motion blurring in general.

In a first landmark-based evaluation, the 4D-MMM achieved an average prediction error (TRE) for the motion between EI and EE images of 3.3 ± 1.6 mm. The model was built based on lungs with intact respiratory dynamics. It was shown that the prediction precision is significantly lower for lungs affected by large tumors (4.0 ± 2.0 mm). These results indicate (at least for the 10 lung tumor patients considered) that large tumors seem to considerably influence respiratory lung dynamics. This finding is in agreement with Plathow *et al.* [49]. Comparing our results to a biophysical finite element (FEM) approach for patient-specific modeling of respiratory lung motion [53], we notice that the 4D-MMM-based prediction quality is only slightly worse for intact lungs (FEM approach: 2.9 ± 1.6 mm) and in the

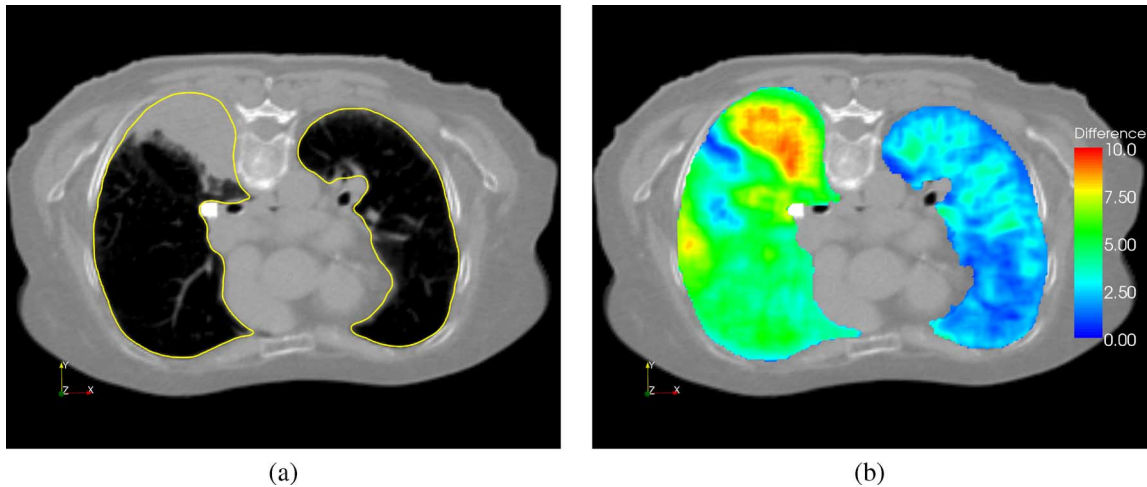


Fig. 8. Difference between lung motion estimated by patient-specific registration and lung motion predicted by the 4D-MMM. (a) CT slice of patient 10 with lung contour (yellow) and tumor adhering to the posterior chest wall. (b) Magnitude of the difference between the individual motion field computed by intra-patient registration and the model-based predicted motion field for this slice. Left lung shows intact lung motion, dynamics of the right lung is impaired by the large tumor.

same order for lungs impaired by large tumors (FEM approach: 4.4 ± 2.5 mm). However, the finite element approach presented in [53] relies on patient-specific 4D images.

In addition, we applied the 4D-MMM to predict patient-specific tumor motions. No correlation between prediction accuracy and tumor size or tumor motion amplitude could be detected (at least for our test data sets). We revealed that tumors adhering to non-lung structures degrade local lung dynamics significantly and model-based prediction accuracy is decreased for these cases. Due to the limited test set, only two patients remain with unimpaired dynamics and with tumors not adhering to a non-lung structure (patient 01 and 07). Therefore, statistically significant conclusions are not possible, although we believe that the motion model is suitable for tumor motion prediction in such a case. From the perspective of the radiation therapy, especially small lung tumors with serious motion amplitudes represent a great challenge for an improved treatment. At the current state, the 4D-MMM could be applied, e.g., to improve RT planning by estimation of the motion impact on dose distributions.

We further conclude from our results that a statistical respiratory motion model has the capability to provide valuable prior knowledge in many fields of applications. We presented two examples of possible applications in radiation therapy and image guided diagnosis. A model-based reduction of uncertainties caused by breathing motion can also be valuable to improve image acquisition or to make subject-specific motion estimation algorithms more robust and precise. Though the current 4D-MMM focuses on inter-patient variations, it can be straightly adapted to intra-patient variations in breathing patterns. Consequently, the model could be applied to improve guidance in gated or tracked RT treatment. An adaptive adjustment of the scaling factor could be realized by additionally monitoring motion indicators (e.g., expiratory volume, diaphragm motion). However, for such a clinical implementation numerous obstacles have to be overcome, which are beyond the scope of this paper. Here, we explored the principle possibilities and restrictions of the model and showed that it yields a reason-

able prediction quality. Moreover, we think that there should be many other potential clinical applications besides the field of radiation therapy, because the modeling techniques can also be adapted to other organs and other dynamic processes in the body (e.g., heart motion or respiration induced liver motion).

Currently, the statistical motion model represents the average motion in the training population. In a preliminary study, the influence of size and composition of the training data set on modeling accuracy was investigated. Further, first steps were done to include the variability of the motion into the model [54]. This will be a main focus of our future work. Here, the Log-Euclidean framework provides a suitable instrument for more detailed inter-patient statistics, like e.g., a principal geodesic analysis of the diffeomorphic transformations describing the patient-specific breathing motion. To ensure reasonable statistics and to improve the accuracy of the motion model, we will increase the number of subjects and the number of breathing states included. The quality of the motion model and the model-based prediction accuracy is mainly influenced by the accuracy of the registration steps involved, and the assessment of the patient-atlas registration is an essential task. However, evaluation of such an inter-subject registration is difficult and will be one focus of our future research. Another focus of research involves investigating the viability of the model in different fields of application.

ACKNOWLEDGMENT

The authors would like to thank D. Low and W. Lu from the Washington University School of Medicine, St. Louis, MO, for providing the 4D CT data.

REFERENCES

- [1] P. J. Keall *et al.*, "The management of respiratory motion in radiation oncology report of AAPM task group 76," *Med. Phys.*, vol. 33, no. 10, pp. 3874–3900, 2006.
- [2] E. C. Ford, G. S. Mageras, E. Yorke, and C. C. Ling, "Respiration-correlated spiral CT: A method of measuring respiratory-induced anatomic motion for radiation treatment planning," *Med. Phys.*, vol. 30, no. 1, pp. 88–97, 2003.

- [3] P. J. Keall, S. Joshi, S. S. Vedam, J. V. Siebers, V. R. Kini, and R. Mohan, "Four-dimensional radiotherapy planning for DMLC-based respiratory motion tracking," *Med. Phys.*, vol. 32, no. 4, pp. 942–951, 2005.
- [4] T. Guerrero, K. Sanders, E. Castillo, Y. Zhang, L. Bidaut, T. Pan, and R. Komaki, "Dynamic ventilation imaging from four-dimensional computed tomography," *Phys. Med. Biol.*, vol. 51, no. 4, pp. 777–791, 2006.
- [5] J. M. Reinhardt, K. Ding, K. Cao, G. E. Christensen, E. A. Hoffman, and S. V. Bodas, "Registration-based estimates of local lung tissue expansion compared to Xenon CT measures of specific ventilation," *Med. Image Anal.*, vol. 12, no. 6, pp. 752–763, 2008.
- [6] D. Sarut, V. Boldea, S. Migué, and C. Ginestet, "Simulation of four-dimensional CT images from deformable registration between inhale and exhale breath-hold CT scans," *Med. Phys.*, vol. 33, no. 3, pp. 605–617, 2006.
- [7] S. A. Nehmeh, Y. E. Erdi, T. Pan, E. Yorke, G. S. Mageras, K. E. Rosenzweig, H. Schoder, H. Mostafavi, O. Squire, A. Pevsner, S. M. Larson, and J. L. Humm, "Quantitation of respiratory motion during 4D-PET/CT acquisition," *Med. Phys.*, vol. 31, no. 6, pp. 1333–1338, 2004.
- [8] S. S. Vedam, P. J. Keall, A. Docef, D. A. Todor, V. R. Kini, and R. Mohan, "Predicting respiratory motion for four-dimensional radiotherapy," *Med. Phys.*, vol. 31, no. 8, pp. 2274–2283, 2004.
- [9] J. M. Blackall, S. Ahmad, M. E. Miquel, J. R. McClelland, D. B. Landau, and D. J. Hawkes, "MRI-based measurements of respiratory motion variability and assessment of imaging strategies for radiotherapy planning," *Phys. Med. Biol.*, vol. 51, no. 17, pp. 4147–4169, 2006.
- [10] D. A. Low, P. J. Parikh, W. Lu, J. F. Dempsey, S. H. Wahab, J. P. Hubenschmidt, M. M. Nystrom, M. Handoko, and J. D. Bradley, "Novel breathing motion model for radiotherapy," *Int. J. Radiat. Oncol. Biol. Phys.*, vol. 63, no. 3, pp. 921–929, 2005.
- [11] J. R. McClelland, J. M. Blackall, S. Tarte, A. C. Chandler, S. Hughes, S. Ahmad, D. B. Landau, and D. J. Hawkes, "A continuous 4D motion model from multiple respiratory cycles for use in lung radiotherapy," *Med. Phys.*, vol. 33, no. 9, pp. 3348–3358, 2006.
- [12] C. Coolens, S. Webb, H. Shirato, K. Nishioka, and P. M. Evans, "A margin model to account for respiration-induced tumour motion and its variability," *Phys. Med. Biol.*, vol. 53, no. 16, pp. 4317–4330, 2008.
- [13] T. Neicu, H. Shirato, Y. Seppenwoolde, and S. B. Jiang, "Synchronized moving aperture radiation therapy (SMART): Average tumour trajectory for lung patients," *Phys. Med. Biol.*, vol. 48, no. 5, pp. 587–598, 2003.
- [14] R. Chandrasekara, A. Rao, G. Sanchez-Ortiz, R. Mohiaddin, and D. Rueckert, "Construction of a statistical model for cardiac motion analysis using nonrigid image registration," in *Proc. Information Processing in Medical Imaging*, ser. Lecture Notes in Computer Science, G. Goos, J. Hartmanis, and J. van Leeuwen, Eds. New York: Springer, 2003, vol. 2732, pp. 599–610.
- [15] D. Perperidis, R. Mohiaddin, and D. Rueckert, "Construction of a 4D statistical atlas of the cardiac anatomy and its use in classification," in *Proc. Med. Image Computing and Computer-Assisted Intervent. (MICCAI 2005)*, ser. Lecture Notes in Computer Science, J. S. Duncan and G. Gerig, Eds. New York: Springer, 2005, vol. 3750, pp. 402–410.
- [16] A. Rao, R. Chandrasekara, G. Sanchez-Ortiz, R. Mohiaddin, P. Aljabar, J. Hajnal, B. Puri, and D. Rueckert, "Spatial transformation of motion and deformation fields using nonrigid registration," *IEEE Trans. Med. Imag.*, vol. 23, no. 9, pp. 1065–1076, Sep. 2004.
- [17] T. A. Sundaram, B. B. Avants, and J. C. Gee, "A dynamic model of average lung deformation using capacity-based reparameterization and shape averaging of lung mr images," in *Proc. Med. Image Computing and Computer-Assisted Intervent. (MICCAI 2004)*, ser. Lecture Notes in Computer Science, C. Barillot, D. R. Haynor, and P. Hellier, Eds. New York: Springer, 2004, vol. 3217, pp. 1000–1007.
- [18] V. Arsigny, "Processing data in lie groups: An algebraic approach. application to non-linear registration and diffusion tensor MRI" Ph.D. dissertation, École Polytechnique, Palaiseau, France, Nov. 2006 [Online]. Available: http://www.sop.inria.fr/asclepios/Publications/Arsigny/arsigny_phd.pdf
- [19] T. Vercauteren, X. Pennec, A. Perchant, and N. Ayache, "Diffeomorphic demons: Efficient non-parametric image registration," *Neuroimage*, vol. 45, no. 1, pp. S61–S72, 2008.
- [20] V. Arsigny, O. Commowick, X. Pennec, and N. Ayache, "A log-Euclidean framework for statistics on diffeomorphisms," in *Proc. Med. Image Computing and Computer-Assisted Intervent. (MICCAI 2006)*, ser. Lecture Notes in Computer Science, R. Larsen, M. Nielsen, and J. Sporring, Eds. New York: Springer, Oct. 2–4, 2006, vol. 4190, pp. 924–931.
- [21] M. F. Beg, M. I. Miller, A. Trounev, and L. Younes, "Computing large deformation metric mappings via geodesic flows of diffeomorphisms," *Int. J. Comp. Vis.*, vol. 61, no. 2, pp. 139–157, 2005.
- [22] X. Pennec, "Intrinsic statistics on riemannian manifolds: Basic tools for geometric measurements," *J. Math. Imag. Vis.*, vol. 25, no. 1, pp. 127–154, 2006.
- [23] D. A. Low, M. Nystrom, E. Kalinin, P. Parikh, J. F. Dempsey, J. D. Bradley, S. Mutic, S. H. Wahab, T. Islam, G. Christensen, D. G. Politte, and B. R. Whiting, "A method for the reconstruction of four-dimensional synchronized ct scans acquired during free breathing," *Med. Phys.*, vol. 30, no. 6, pp. 1254–1263, 2003.
- [24] W. Lu, P. J. Parikh, I. M. El Naqa, M. M. Nystrom, J. P. Hubenschmidt, S. H. Wahab, S. Mutic, A. K. Singh, G. E. Christensen, J. D. Bradley, and D. A. Low, "Quantitation of the reconstruction quality of a four-dimensional computed tomography process for lung cancer patients," *Med. Phys.*, vol. 32, pp. 890–901, 2005.
- [25] J. Ehrhardt, R. Werner, D. Säring, T. Frenzel, W. Lu, D. Low, and H. Handels, "An optical flow based method for improved reconstruction of 4D CT data sets acquired during free breathing," *Med. Phys.*, vol. 34, no. 2, pp. 711–721, 2007.
- [26] J. Ehrhardt, D. Säring, and H. Handels, "Structure-preserving interpolation of temporal and spatial image sequences using an optical flow based method," *Methods Inf. Med.*, vol. 46, pp. 300–307, 2007.
- [27] J.-M. Peyrat, H. Delingette, M. Sermesant, X. Pennec, C. Xu, and N. Ayache, "Registration of 4D time-series of cardiac images with multichannel diffeomorphic demons," in *Proc. Med. Image Computing and Computer-Assisted Intervent. (MICCAI 2008)*, ser. Lecture Notes in Computer Science, D. N. Metaxas, L. Axel, G. Fichtinger, and G. Székely, Eds. New York: Springer, 2008, vol. 5241, pp. 972–979.
- [28] A. Trounev, "Diffeomorphisms groups and pattern matching in image analysis," *Int. J. Comp. Vis.*, vol. 28, no. 3, pp. 213–221, 1998.
- [29] J. Ashburner, "A fast diffeomorphic image registration algorithm," *Neuroimage*, vol. 38, no. 1, pp. 95–113, 2007.
- [30] M. Hernandez, M. N. Bossa, and S. Olmos, "Registration of anatomical images using paths of diffeomorphisms parameterized with stationary vector field flows," *Int. J. Comp. Vis.*, vol. 85, pp. 291–306, 2009.
- [31] S. Marsland and C. J. Twining, "Constructing an atlas for the diffeomorphism group of a compact manifold with boundary, with application to the analysis of image registrations," *J. Comput. Appl. Math.*, vol. 222, no. 2, pp. 411–428, 2008.
- [32] T. Vercauteren, X. Pennec, A. Perchant, and N. Ayache, "Symmetric logdomain diffeomorphic registration: A demons-based approach," in *Proc. Med. Image Computing and Computer-Assisted Intervent. (MICCAI 2008)*, ser. Lecture Notes in Computer Science, D. N. Metaxas, L. Axel, G. Fichtinger, and G. Székely, Eds. New York: Springer, 2008, vol. 5241, pp. 754–761.
- [33] J. Modersitzki, *Numerical Methods for Image Registration*. New York: Oxford Univ. Press, 2003.
- [34] J.-P. Thirion, "Image matching as a diffusion process: An analogy with Maxwell's demons," *Med. Image Anal.*, vol. 2, no. 3, pp. 243–260, 1998.
- [35] P. Cachier, E. Bardinet, D. Dormont, X. Pennec, and N. Ayache, "Iconic feature based nonrigid registration: The pasha algorithm," *Comput. Vis. Image Understand.*, vol. 89, no. 2–3, pp. 272–298, 2003.
- [36] J. Weickert, B. M. T. H. Romeny, and M. A. Viergever, "Efficient and reliable schemes for nonlinear diffusion filtering," *IEEE Trans. Image Process.*, vol. 7, no. 3, pp. 398–410, Mar. 1998.
- [37] A. Guimond, J. Meunier, and J.-P. Thirion, "Average brain models: A convergence study," *Comput. Vis. Image Understand.*, vol. 77, no. 2, pp. 192–210, 2000.
- [38] S. Joshi, B. Davis, M. Jomier, and G. Gerig, "Unbiased diffeomorphic atlas construction for computational anatomy," *Neuroimage*, vol. 23, pp. S151–S160, 2004.
- [39] D. Rueckert, A. Frangi, and J. Schnabel, "Automatic construction of 3D statistical deformation models of the brain using nonrigid registration," *IEEE Trans. Med. Imag.*, vol. 22, no. 8, pp. 1014–1025, Aug. 2003.
- [40] M. Vaillant, M. I. Miller, L. Younes, and A. Trounev, "Statistics on diffeomorphisms via tangent space representations," *Neuroimage*, vol. 23, pp. S161–S169, 2004.
- [41] M. I. Miller and L. Younes, "Group actions, homeomorphisms, and matching: A general framework," *Int. J. Comp. Vis.*, vol. 41, no. 1–2, pp. 61–84, 2001.
- [42] V. Arsigny, P. Fillard, X. Pennec, and N. Ayache, "Geometric means in a novel vector space structure on symmetric positive-definite matrices," *SIAM J. Matrix Anal. Appl.*, vol. 29, no. 1, pp. 328–347, 2007.
- [43] M. N. Bossa and S. O. Gasso, "A new algorithm for the computation of the group logarithm of diffeomorphisms," in *Proc. Int. Workshop Math. Foundations Computat. Anatomy (MFCA 2008)*, X. Pennec and S. Joshi, Eds., New York, 2008, pp. 13–23.

- [44] S. Hu, E. Hoffman, and J. Reinhardt, "Automatic lung segmentation for accurate quantitation of volumetric X-ray CT images," *IEEE Trans. Med. Imag.*, vol. 20, no. 6, pp. 490–498, Jun. 2001.
- [45] B. Avants and J. C. Gee, "Geodesic estimation for large deformation anatomical shape averaging and interpolation," *Neuroimage*, vol. 23, pp. S139–S150, 2004.
- [46] R. Werner, J. Ehrhardt, T. Frenzel, D. Säring, W. Lu, D. Low, and H. Handels, "Motion artifact reducing reconstruction of 4D CT image data for the analysis of respiratory dynamics," *Methods Inf. Med.*, vol. 46, no. 3, pp. 254–260, 2007.
- [47] Y. Yin, E. A. Hoffman, and C.-L. Lin, "Mass preserving nonrigid registration of CT lung images using cubic B-spline," *Med. Phys.*, vol. 36, no. 9, pp. 4213–4222, 2009.
- [48] P. J. Besl and N. D. McKay, "A method for registration of 3-D shapes," *IEEE Trans. Pattern Anal. Mach. Intell.*, vol. 14, no. 2, pp. 239–256, Feb. 1992.
- [49] C. Plathow, C. Fink, S. Ley, M. Puderbach, M. Eichinger, I. Zuna, A. Schmäh, and H. Kauczor, "Measurement of tumor diameter-dependent mobility of lung tumors by dynamic MRI," *Radiother. Oncol.*, vol. 73, pp. 349–354, 2004.
- [50] ICRU, Report 62: Prescribing, Recording and Reporting Photon Beam Therapy (Supplement to ICRU Report 50) Int. Commission Radiation Units Measurements, Tech. Rep., 1999.
- [51] R. Kashani, M. Hub, J. M. Balter, M. L. Kessler, L. Dong, L. Zhang, L. Xing, Y. Xie, D. Hawkes, J. A. Schnabel, J. McClelland, S. Joshi, Q. Chen, and W. Lu, "Objective assessment of deformable image registration in radiotherapy: A multi-institution study," *Med. Phys.*, vol. 35, no. 12, pp. 5944–5953, 2008.
- [52] R. Castillo, E. Castillo, R. Guerra, V. E. Johnson, T. McPhail, A. K. Garg, and T. Guerrero, "A framework for evaluation of deformable image registration spatial accuracy using large landmark point sets," *Phys. Med. Biol.*, vol. 54, no. 7, pp. 1849–1870, 2009.
- [53] R. Werner, J. Ehrhardt, R. Schmidt, and H. Handels, "Patient-specific finite element modeling of respiratory lung motion using 4D CT image data," *Med. Phys.*, vol. 35, no. 5, pp. 1500–1511, 2009.
- [54] J. Ehrhardt, R. Werner, A. Schmidt-Richberg, and H. Handels, "A statistical shape and motion model for the prediction of respiratory lung motion," in *Medical Imaging 2010: Image Processing*, B. M. Dawant and D. R. Haynor, Eds. Bellingham, WA: SPIE, 2010, vol. 7623, p. 762353.